Geomorphology 334 (2019) 29–43

Contents lists available at ScienceDirect

Geomorphology

journal homepage: www.elsevier.com/locate/geomorph

Invited research article

Experimental investigation on the longitudinal evolution of landslide dam breaching and outburst floods

Gordon G.D. Zhou [a,b], Mingjun Zhou [a,b,*], Mandira Singh Shrestha [c], Dongri Song [a,b], Clarence E. Choi [d,e,f], Kahlil Fredrick E. Cui [a,b], Ming Peng [g], Zhenming Shi [g], Xinghua Zhu [h], Huayong Chen [a,b]

[a] Key Laboratory of Mountain Hazards and Earth Surface Process, Institute of Mountain Hazards and Environment, Chinese Academy of Sciences (CAS), Chengdu, China
[b] University of Chinese Academy of Sciences, Beijing, China
[c] International Centre for Integrated Mountain Development (ICIMOD), Nepal
[d] Department of Civil and Environmental Engineering, The Hong Kong University of Science and Technology, Hong Kong Special Administrative Region
[e] The HKUST Jockey Club Institute for Advanced Study, Hong Kong Special Administrative Region
[f] HKUST Fok Ying Tung Graduate School, Nansha, China
[g] Key Laboratory of Geotechnical and Underground Engineering of Ministry of Education, Department of Geotechnical Engineering, Tongji University, Shanghai, China
[h] College of Geological Engineering and Surveying of Chang'an University, Key Laboratory of Western China Mineral Resources and Geological Engineering, Xi'an, China

ARTICLE INFO

Article history:
Received 16 October 2018
Received in revised form 23 February 2019
Accepted 23 February 2019
Available online 26 February 2019

Keywords:
Landslide dam
Overtopping failure
Hydrograph
Erosion rate

ABSTRACT

Accurate prediction of the evolution of a landslide dam that is breached due to overtopping failure is necessary to estimate the outflow hydrograph and the resulting inundation. In this study, physical flume tests on the breaching of landslide dams were conducted. A wide grain size distribution with unconsolidated dam material was used. Dam breaching was initiated by cutting a notch across the crest of the dam adjacent to the side wall of the flume. This allowed water to escape from the dam while a steady inflow of water was continuously supplied upstream. The effects of upstream inflow on the timescales and magnitudes of the peak discharges and the time to inflection point were also investigated. Experimental results reveal that the whole hydrodynamic process of dam breaching can be divided into three stages defined by clear inflection points and peak discharge. A new longitudinal evolution model is proposed. This model captures the initial increase of the soil erosion rate (of landslide dam) and its subsequent decrease along the longitudinal direction. In addition, a linear relationship between the soil erosion rate and shear stress (of water flow) was observed and this is similar to that observed in large-scale natural landslide dams. Furthermore, soil erosion resistances (of landslide dam) against water flow above are observed to increase with the concentration of entrained sediments along the flow direction.

1. Introduction

Landslide dams are a natural occurrence, and they commonly form because of the blockage of river channels by mass earth movements (Costa and Schuster, 1988; Casagli et al., 2003). Catastrophic outburst floods, following rapid landslide dam failure, have long been recognized as natural hazards (King et al., 1989; Shang et al., 2003; Huang, 2009). The primary failure mechanism is overtopping (Korup, 2004). For example, the Tangjiashan landslide dam, induced by the M_S 8.0 Wenchuan earthquake (2008), formed a dammed lake with a total volume of 316 million m^3 (Liu et al., 2009). This dammed lake threatened >1.3 million people residing in the downstream areas. Rapid water flows discharging in gullies under intense rainfall can induce landslide dam failures along steep sloping channels (Cui et al., 2013). On the 8th of August 2010, a large-scale debris flow event was triggered by a cascading failure of landslide dams upstream, along the sloping channels, of Zhouqu County, China (Cui et al., 2013; Zhou et al., 2013). The debris flow destroyed all buildings along its flow path. The residual deposit flooded half of the urban area for over 20 days. Recently a catastrophic landslide, which was triggered by heavy rainfalls, has dammed the Jinsha River (upstream of the Yangtze River), China, on the 11th of October, 2018. The volume of dammed lake was estimated to be >150 million m^3. The overtopping failure began on the morning of the 12th of October, resulting to a maximum flood peak discharge of 7000 m^3/s along the downstream area. In addition, studies have suggested that landslide dams have a proportionately larger role in controlling river evolution over timescales of 10^4–10^5 years in mountain terrains (Korup, 2006; Korup et al., 2010; Walsh et al., 2012; van Gorp et al., 2016; J. Liu et al., 2018; W. Liu et al., 2018). Therefore, a clear understanding of the

* Corresponding author at: Key Laboratory of Mountain Hazards and Earth Surface Process, Institute of Mountain Hazards and Environment, Chinese Academy of Sciences (CAS), Chengdu, China.
E-mail address: mjzhou@imde.ac.cn (M. Zhou).

https://doi.org/10.1016/j.geomorph.2019.02.035
0169-555X/

whole landslide dam overtopping failure process and the resulting flood is an important area of study in the prediction and mitigation of such hazards.

Landslide dam disaster prevention and mitigation basically involves two primary components. One is disaster forecasting, which focuses on the premonitory of failure and failure modes (overtopping failure/ slope failure) (Jiang et al., 2018; Wang et al., 2018). Another component involves a detailed study of the dam-breach disaster process. The latter is primarily focused on an understanding of two vital elements: (i) changes in breach geometry with time and (ii) flooding (Coleman et al., 2002; Hanson et al., 2005; Hunt et al., 2005; Cao et al., 2011; Walder et al., 2015; Itoh et al., 2018). When studying the changes to a cross-section of a breach, trapezoidal/ rectangular/ parabolic cross-sections occur under different initial conditions (e.g., dam geometry, granular materials and inflow discharge). Correspondingly, different models have been proposed (e.g., Cristofano, 1965; Fread, 1988; Visser, 1998) and have been closely evaluated (e.g., Coleman et al., 2002; Walder et al., 2015). For main flows parallel to the dam axis, such as the case with embankments/levees, asymmetries in the breach cross -section direction due to the perpendicular overtopping flow are observed (cf. Rifai et al., 2017). Correspondingly, Wu et al. (2018) further proposed asymmetry coefficients with values that fall between 2.2 and 3.3 (2.2–2.6 for Non-cohesive sand levee; 2.7–3.3 for cohesive clay levee). In contrast, breach geometries for flows along the longitudinal direction, as in the case of landslide dams, have yet to be elucidated. As a result, even when back-analyzing a single dam failure, several different longitudinal evolution models can be inferred. For example, Chang and Zhang (2010) defined the overtopping failure of the Tangjiashan landslide dam, using a theoretical model reported by Powledge et al. (1989). This model assumes that the downstream slope angles rapidly increases until a constant critical soil friction angle is achieved. The erosion rate, $E = \frac{dh_j}{dt}$, which expresses the change in the erosion depth h_j relative to the change in time t, is then assumed to remain the same at each time step in such a way that the critical angle is constant (Fig. 1a). However, the results from this model are inconsistent with the observed initial and final mechanisms of the Tangjiashan landslide dam failure (cf. Liu et al., 2009; Ning et al., 2010). Zhong et al. (2018) further revised the model by assuming that the erosion rate decreases along the flow direction (Fig. 1b). Each of these models leads to different hydrological processes and both exhibit differences from the actual event. During the overtopping failure process, the potential energy of the stored water should gradually be transformed into kinetic energy as water flows downslope. As the flow velocity increases, the pertinent soil erosion rate which is closely correlated to flow velocity should also increase (Cao, 1999; Carrivick, 2010; G.G.D Zhou et al., 2015; X.Q. Zhou et al., 2015). Thus, the distribution of erosion rate on the sloping bed should increase, contrary to existing models (cf. Chang and Zhang, 2010; Zhong et al., 2018).

The erosion rate on the downstream sloping bed of landslide dam is directly affected by the shear stress (τ) exerted by the water flow on the sloping bed and the pertinent sediment erosion resistance (τ_c). When shear stress of water flow (τ) is higher than the soils erosion resistance (τ_c), granular materials comprising the landslide dam can be entrained into the outburst floods. These sediments are transported to the downstream areas. The erosion process is represented by the erosion rate (E). There are several ways to calculate erosion rate E (e.g., Shields, 1936; Yalin, 1977; Julien, 1995). For sediment transport

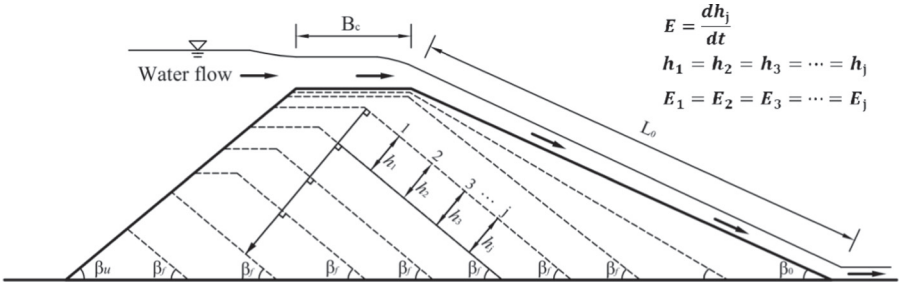

(a)

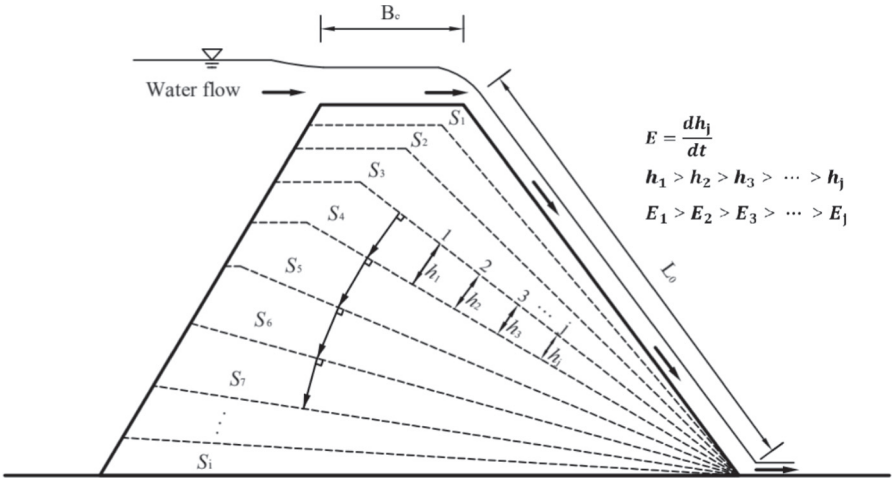

(b)

Fig. 1. (a) Evolution of longitudinal breach profile of the landslide dam due to overtopping failure by Chang and Zhang (2010) (Modified); (b) evolution of longitudinal breach profile of the landslide dam due to overtopping failure by Zhong et al. (2018) (Modified). B_c means the width of dam crest and L_0 is the length of downstream slope.

in rivers, an exponential relationship between E, τ, and τ_c has been proposed (Roberts et al., 1998) as follows:

$$E = a(\tau - \tau_c)^b \quad (1)$$

where parameters, a and b (both > 0) depend on different initial conditions (Walder, 2016). When b = 1, the erosion rate becomes a function of the difference between the shear stress (τ) and the erosion resistance (τ_c) with a as the coefficient of proportionality (Hanson and Cook, 1997). Gaucher et al. (2010) and Wu et al. (2018) presented laboratory results indicating that this exponential relationship of Eq. (1) can be adopted to study crest failure of artificial/manual dams due to overtopping flows. The main difference between manmade and landslide dams is that landslide dams are formed by an unconsolidated heterogeneous mixture of earth or rock debris in a naturally unstable state and the granular material possess a wide range of particle sizes (Costa and Schuster, 1988; Casagli et al., 2003). Correspondingly, the relevance of the presented erosion rate equation (Eq. (1)) for the overtopping failure process of landslide dams remains unclear.

Another problem is whether the relationship between the erosion rate and the shear stress for one cross-section of the dam can be applied to the rest of the dam. This problem has not yet been addressed in previous research (cf. Chang and Zhang, 2010; Wu, 2013; Liu and He, 2017; Zhong et al., 2018). The underlying assumption is that the process of outburst erosion is considered as clear water erosion along all cross-sections. However, the concentration of solids (C_s) in an outburst flow varies along the longitudinal direction. Wang and Xu (1998) showed that the erosion rate is larger if the flow carries no sediment ($C_s = 0$) and the erosion rate decreases with increasing sediment concentration since more entrained sediment can reduce the carrying capacity of the flow. Moreover, when the sediment load is equal to the flow capacity, the average erosion rate of the flow will be zero even when the flow velocity is relatively high. The following argument, among others, provides a basis as to why the assumption of clear water erosion along the water direction may lead to inaccuracies in modeling landslide dam overtopping failures. This would be true for actual landslide dams with much larger widths (along the river direction). Some examples include 803 m of Tangjiashan landslide dam (Xu et al., 2009), 1300 m of Diexi landslide dam (Costa and Schuster, 1988) and 2350 m of Yigong landslide dam (Peng and Zhang, 2012).

This paper presents the results of landslide dam overtopping experiments for four different upstream inflow discharges (2.0×10^{-3}, 3.0×10^{-3}, 5.3×10^{-3}, 6.9×10^{-3} m^3/s). These experiments were designed to: (i) set up an evolution model of the longitudinal profile for overtopping failure of landslide dams, especially for those located in mountainous areas; (ii) propose a relationship between erosion rate and shear stress suitable for outburst flows; and (iii) investigate whether the proposed erosion relationship is applicable along the longitudinal direction of landslide dams. Evaluation of the longitudinal morphology was done using photogrammetric methods, complemented by a camera at the side of the model. Although there exists landslide dams that have failed due to groundwater seepage or piping (Costa and Schuster, 1988), discussion thereof is outside the scope of this paper. To reduce the effects of seepage or piping on the dam failure process, the water in the reservoir was allowed to fill rapidly.

2. Experimental setup

2.1. Model design

Scaling laws play a crucial role in designing physical model tests which aim to understand the behavior of landslides, debris flows, and other geomorphological phenomena involving grain-fluid mixtures (Iverson, 2015). Costa and Schuster (1988) illustrated that the potential energy of water is an important parameter affecting the dam failure and outburst floods, and it is correlated to the volume of dammed lake (V_l). After field investigation, Korup (2004) suggested that the landslide dam height (H_d) and the volume of the landslide dam (V_d) are two key variables for assessing landslide dam stability and the risks of further induced flooding. Therefore, both the dam geometry and the dammed lake volume should be carefully taken into consideration. After a series of dimensional analysis, Peng and Zhang (2012) proposed a set of dimensionless numbers - $\frac{H_d}{W_d}$, $\frac{V_d^{1/3}}{H_d}$, and $\frac{V_l^{1/3}}{H_d}$ - that can be used to define the geometrical characteristics of landslide dams and dammed lakes. These parameters were considered during the dam model design and construction. The ratio of the dam height to its width $\left(\frac{H_d}{W_d}\right)$ defines the slope erosion and controls the velocity of water flow and the pertinent erosion rate. The ratio between the cubic root of the dam volume and height, also known as the dam shape coefficient $\left(\frac{V_d^{1/3}}{H_d}\right)$, reflects the amount of granular material that can be entrained and can influence the breaching duration. The lake shape coefficient $\left(\frac{V_l^{1/3}}{H_d}\right)$ is the ratio between the cube root of the water volume and the dam height. It indicates the potential volume of water that can be poured out to erode the dam, thus influencing the breach size and the outflow discharge. To verify if the experimental dam can represent real large-scale landslide dams, its dimensionless coefficients were evaluated against those of 80 reported landslide dams from different locations of the world, which were formed from rock avalanches, debris flows, and other types of geophysical mass flows (see Fig. 2). The symmetry of the data points of the natural landslide dams in logarithm-linear coordinate system is remarkable in Fig. 2a. This indicates a positive correlation between the volume of dam body and the volume of dammed lake. This positively linear relationship (in logarithm-logarithm terms) between volumes of the landslide dam and the dammed lake,

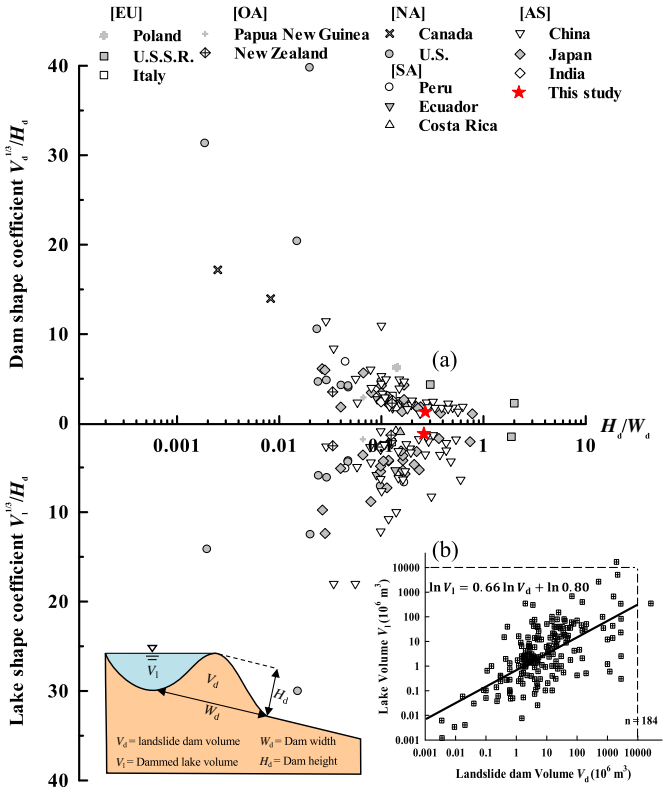

Fig. 2. (a) Ternary plot of landslide-dam dimensionless parameter derived from a worldwide data set (Costa and Schuster, 1988; Korup, 2004; Xu et al., 2009; Yin et al., 2009; Peng and Zhang, 2012); (b) the relationship between landslide dam volume and lake volume (Korup, 2004). ([NA] is North America, [SA] is South America, [EU] is Europe, [OA] is Australia, and [AS] is Asia).

$\ln V_l = 0.66 \ln V_d + \ln 0.80$, was also presented by Korup (2004) (Fig. 2b). The dimensionless coefficients that define the modeled landslide dam presented in this paper fall within the acceptable range of values and can therefore be considered to represent real landslide dams.

2.2. Granular material used in flume model test

The geotechnical behavior of landslide dams (e.g., shear strength) and the dam failure processes are closely correlated to the grain size distribution of the granular materials (cf. Swanson et al., 1986; Casagli et al., 2003). To emulate the poorly-sorted soils of natural landslide dams, the granular materials in the Jiangjia Ravine near Dongchuan Debris Flow Observation and Research Station (DDFORS), Yunnan Province of China were used to construct the modeled landslide dams. Fig. 3 shows the grain-size distribution of the modeled landslide dams. The diameters of fine particles (which have passed through a 0.25 mm sieve) were measured using a Malvern Mastersizer 2000 instrument. This device is designed to measure the size of small particles and the distribution of these sizes within a sample, based on the laser diffraction principle and on known particle size distribution statistics (Malvern Instruments Ltd, 2007). Considering the grain size effect, the particles with diameters larger than 20 mm were removed in all tests. Sediment samples in all experimental sets had mean grain diameters of $d_{50} =$ 0.85 mm. A dimensionless measure of the spread in the grain-size distribution, $\sigma_g = \frac{d_{84}}{d_{16}} = 75$ (Walder, 2016) represents a wide grain size range of granular materials for landslide dams (Fig. 3). The unit weight and friction angle of the solid materials were measured to be $\rho_s =$ 2650 kg/m^3 and $\varphi = 30°$respectively (cf. Zhou and Ng, 2010).

2.3. Experiment setup and test procedures

A large flume was constructed near DDFORS, in Dongchuan District, Yunnan Province, China (N26°14′, E103°08′). The flume consisted of a straight concrete channel (45 m long, 0.7 m wide and 1.4 m deep), inclined at 12° to the horizontal (Fig. 4a) (G.G.D Zhou et al., 2015; X.Q. Zhou et al., 2015). At the lower end of the flume, the slope opened onto a horizontal concrete plane. The flume walls and run-out area were made of smooth cement. Along the walls of the flume are five 1 m wide reinforced glass windows, which allow the observation of the dam overtopping process. A water container, with a capacity of 12 m^3, was connected to the top of the flume through a channel with rows of saw-teeth, which dissipated any turbulent energy from the released upstream flow, effectively minimizing the turbulence effects experienced by the dam downstream.

To simulate unconsolidated unstable blockages, granular materials were well-mixed each time and poured from the same height into the sloping channel to form landslide dams that were in accordance with the natural repose angle of soils. Manual compaction was adopted to ensure that the void ratio (0.78–0.80) of each layer was consistent with field conditions which were mostly in the range of 0.59–1.11 (cf. Chang and Zhang, 2010). This process was repeated until the desired dam geometry was achieved. After the dam crest was smoothed and leveled, a rectangular notch ($h_0 \times w_0 = 0.05$ m $\times$ 0.1 m) was excavated on the dam crest, adjacent to the side glass wall (Fig. 4b and c). This ensures that the overtopping failure starts at the same place every time, minimizing variability between different runs of the experiment. The longitudinal evolution of the landslide dam failure process is viewed through the transparent wall, as adopted by Hakimzadeh et al. (2014). After finishing the construction of the dam, all the instruments were simultaneously switched on. The water valve was opened and the upstream flow entered the dammed lake. The upstream inflow rate Q_{in} was large enough to minimize the effect of seepage on the dam failure process. As the water started to flow over the dam crest, tracer particles were dropped in to capture the flow dynamics and to estimate the velocity of the outburst flood (Fig. 4b and d).

In order to capture the longitudinal evolution of landslide dams and outburst floods, three digital video cameras (SONY FDR-AX40, 1440 $\times$ 1080 pixels, 25 fps) and one laser sensor (Leuze, ODSL 30/V-30M-S12) with resolution of $\pm$1 mm were installed above the channel. Another digital video camera (SONY FDR-AX40, 1440 $\times$ 1080 pixels, 25 fps) was positioned on the free side of the glass panel (Fig. 5). Digital video cameras #1, #2 and #3 are set to record the longitudinal evolution of the breach, while camera #1 is set to capture variations of the flow depth as soil erosion progresses and is also used to estimate the flow

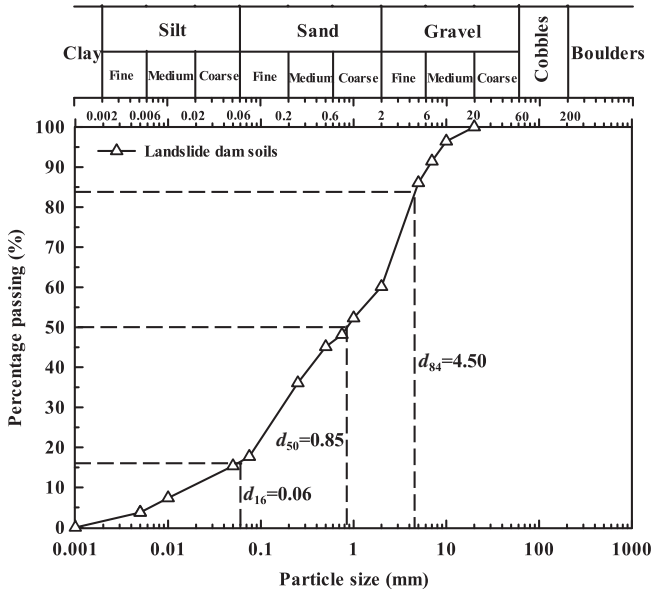

Fig. 3. Grain-size distribution of the modeled landslide dams. A mean size of $d_{50} = 0.85$ mm and dimensionless measure of the spread in the grain-size distribution $\sigma_g = 75$ was adopted in all experimental set-ups.

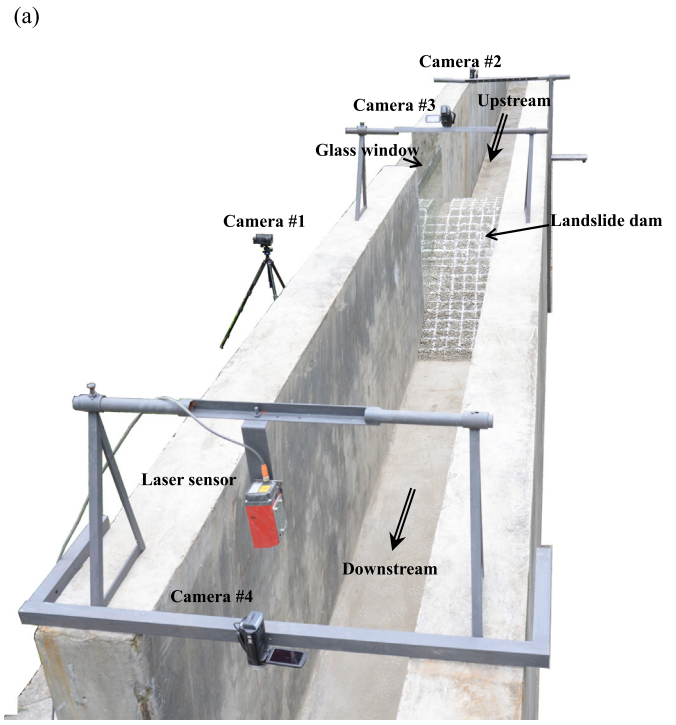

Fig. 4. (a) A front view of the model dam as viewed from the downstream region of the flume, (b) the view from the vantage point of camera #3, (c) detailed dimensions of dam crest cross-section, and (d) side-view from the vantage point of camera #1.

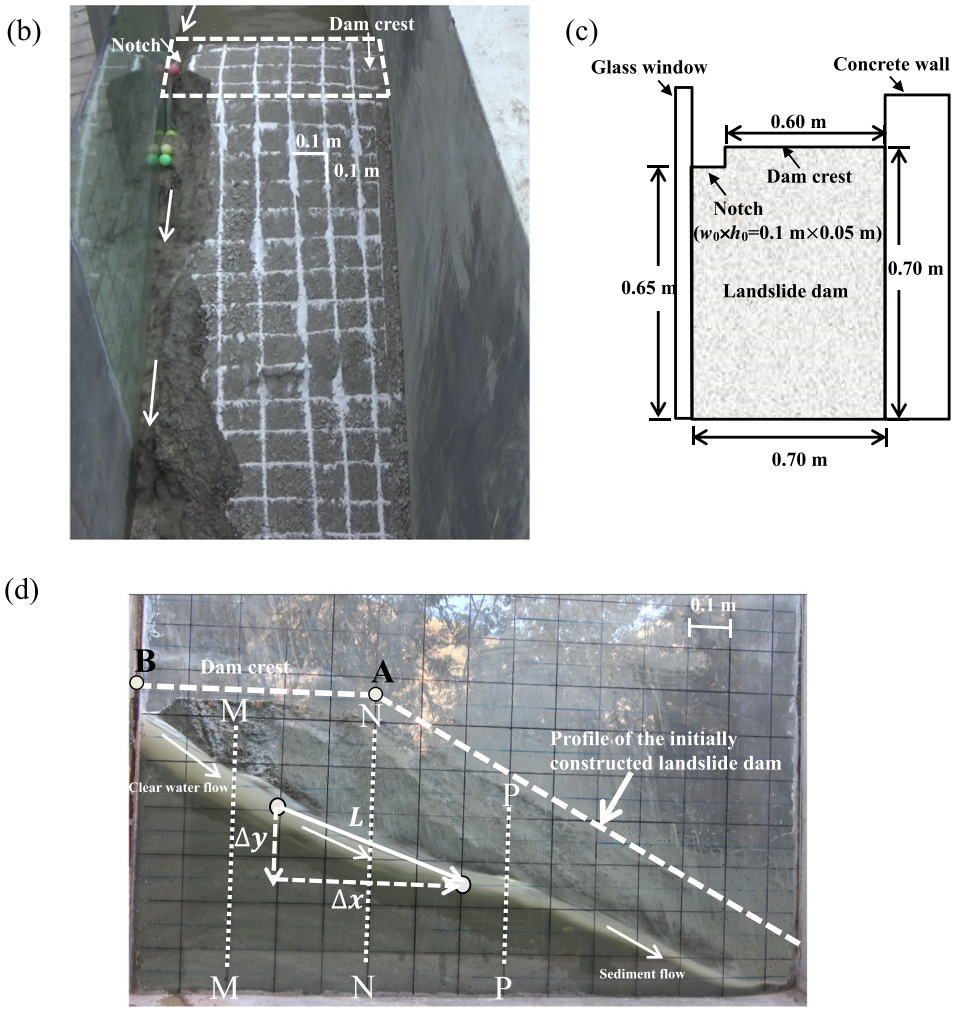

Fig. 4 (*continued*).

velocity from the motion of the tracer particles. Camera #4 is installed to calculate the velocity of the outburst flood. The laser sensor was used to measure the depth of outflow (Gregoretti et al., 2010; Pickert et al., 2011). By combining the data from the laser sensor and the videos from camera #4, the outburst discharge was measured 5 m away from the downstream dam toe. In addition, continuous sampling was adopted during the tests to calculate the changes of the outburst flood density.

In total, four different upstream inflow discharges (2.0×10^{-3}, 3.0×10^{-3}, 5.3×10^{-3}, 6.9×10^{-3} m^3/s) were applied to study the effects of the upstream inflow on the landslide dam breaching process and outburst flooding (see Table 1). Each test has been conducted at least twice to evaluate the repeatability of the results.

2.4. Data analysis

Flow velocities were measured by tracking the trajectory of a tracer particle within a given reference frame centered at a specific point along the dam. Tracer particles were selected so that they do not interfere with the fluid flow. Tracers must be less dense than the fluid they

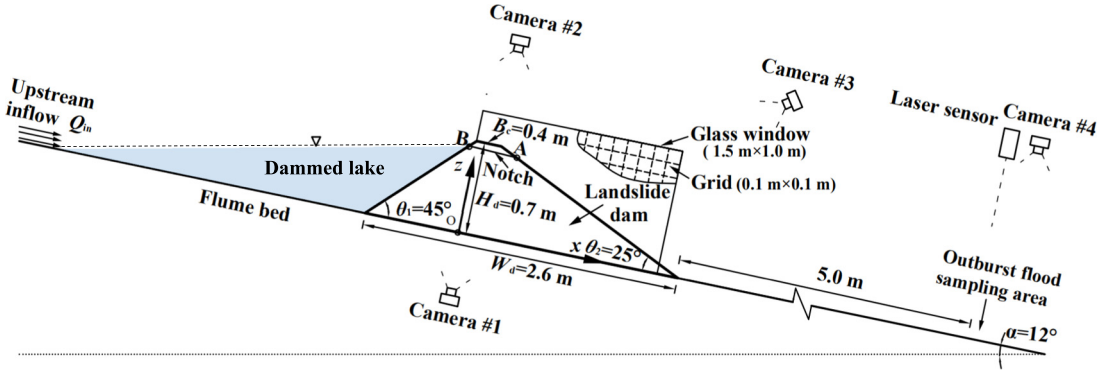

Fig. 5. Schematic diagram of the model dam with the exact dimensions.

Table 1
Test program.

Test ID	Q_{in}[a] ($\times 10^{-3}$ m^3/s)	Q_i[b] ($\times 10^{-3}$ m^3/s)	Q_p[c] ($\times 10^{-3}$ m^3/s)	Δt_1[d] (s)	$\Delta t_1 + \Delta t_2$[e] (s)	β_1[f]	β_2[g]
C-Q2.0	2.0	1.6	14.9	33	51	0.05	0.32
C-Q3.0	3.0	0.7	15.5	17	37	0.01	0.25
C-Q5.3	5.3	2.4	17.3	15	22	0.02	0.40
C-Q6.9	6.9	7.7	18.3	14	20	0.07	0.26

Each test has been repeated twice.
[a] Q_{in} Upstream inflow discharge.
[b] Q_i Discharge at the inflection point.
[c] Q_p Peak discharge.
[d] Δt_1 Time between the first recorded outflow discharge to the inflection point.
[e] $\Delta t_1 + \Delta t_2$ Time between the first recorded outflow discharge to the peak discharge.
[f] $\beta_1 = \frac{\Delta Q_1}{\Delta t}$ Rate of outburst discharge in Stage 1.
[g] $\beta_2 = \frac{\Delta Q_2}{\Delta t}$ Rate of outburst discharge in Stage 2.

flow with so that they can stay afloat, but at the same not too light so as to keep them from being blown away by the air currents that form at the fluid free surface (J. Liu et al., 2018; W. Liu et al., 2018). The particles must also be big enough to be easily visible by the camera so as to prevent peak-locking effects (Baba and Peth, 2012). Based on these considerations, large quantities of colored plastic balls (cellulose acetate) were used in the experiment.

The velocity of a tracer particle was measured by taking the total distance travelled within a pre-defined frame of reference (Δx) and dividing it with the total time it takes for the tracer to travel the span of the reference frame. The particle's travel distance is defined as the difference between an initial and final point $\left(L = \sqrt[2]{\Delta x^2 + \Delta y^2}\right)$ (Fig. 4d). Measurements were observed from snapshots recorded by cameras at a frequency of 25 fps. The said reference frames are centered at certain cross-sections along the dam body labelled M, N, and P (Fig. 4d). Section M is 0.2 m away from the upstream dam crest Point B. Section P is at the middle of the dam 0.8 m away from the upstream crest Point B. Section N is 0.5 m away from the upstream crest Point B which lies in between Sections M and P, coinciding with the downstream dam crest Point A. While the particles are not entirely neutrally buoyant, their calculated velocities were deemed to be good estimates of flow velocity at the representative cross-sections. The size of the reference frame is assumed to affect the resolution of the measured velocities. Correspondingly, an optimal length at which reasonable velocity estimates can be obtained must be determined beforehand. Based on our estimated flow velocity, the maximum velocity can reach nearly 4 m/s in Section P. The lengths of the spatial windows to be tested were set to be Δx =0.1 m, Δx =0.2 m, Δx =0.4 m and Δx =0.6 m (the length of a single grid imprinted on the glass panel on the side of the flume, as seen in Fig. 4d, is 0.1 m). Results show that flow velocities initially increase and then decrease until the flow reaches a relatively steady condition. The velocity of water flow increases gradually along the longitudinal direction (Fig. 6a, b, and c). The maximum velocity was obtained at the Section P (Fig. 6c). The size of reference frame does not significantly affect the measured velocities. However, considering the large flow velocity, the measured values exhibit fluctuations due to the short distances, Δx =0.1 m and Δx =0.2 m, adopted. Meanwhile, the accuracy of resulting from a distance of Δx =0.6 m is relatively low, therefore a distance of Δx =0.4 m was deemed the most appropriate for subsequent measurement and analyses of flow velocities at M, N, and P.

In a similar manner as the measured flow velocities, the measured flow depths were also taken at representative cross sections (Sections M, N, and P). At each section three measurements are obtained at a given time that it takes a tracer particle to span the spatial measurement window. The distance between the free surface and the dam sloping bed is measured flow depth. The results of the three measurements show that the flow depth increases slowly, then abruptly increases before finally decreasing rapidly to 0 (see Fig. 6d, e, and f). It is also noted that the maximum flow depth is obtained at Section M, and that the flow depth decreases correspondingly at N and P. The flow depths decrease along the flow path. The three measurements all reflect the changes in water depth and the result is consistent.

3. Experimental results

3.1. General observations

3.1.1. Longitudinal evolution process of dam breaching

The rapid change of the hydrodynamic conditions during landslide dam breach makes the process of dam failure very complex. The initial time of dam breaching t_0 = 0 s, begins when water starts to travel along the initial notch and eventually reaches the downstream crest, Point A (Fig. 7a). This is where the overtopping failure of landslide dam initially occurs. At this stage, however, the water flows are insufficient to erode the soils, the overtopping flow depth is still shallow and the flow velocity is still quite small (Fig. 6). As such, most of the sediment transport is still confined at the area immediately below dam crest Point A (Fig. 7b). Most of the eroded material at this point does not travel very far and is simply deposited at the nearest point downstream (Fig. 7c). As the upstream inflow continues to supply flowing water, the flow velocity gradually increases and so does the erosion rate. The fine particles are more easily eroded and entrained into the outburst floods, resulting in an increase of the suspension in the water. Outburst floods start to develop, further entraining the soil and increasing the amount of suspended particles in the water. By this point, the inflowing water erodes both the downstream region (from Point A to the toe of the dam) and some parts of the upstream crest bounded by Points A and B (Fig. 7c and d). Before t_3 = 33 s (Fig. 7d), the geometry of the sloping bed is relatively irregular. When the erosion point reaches Point B at t_4 = 43 s (Fig. 7e), the dam crest completely collapses and the water level of the dammed lake quickly decreases as larger amounts of water are released downstream. This further accelerates the erosion process along the dam surface. From Fig. 7e, the water flow at the overtopped dam crest is clear. However, it becomes murky and sediment-laden near the dam toe as it entrains soil particles along its path. At the time t_5 = 51 s (Fig. 7f), the depth of the water starts to decline and the geometry of the sloping bed begins to smoothen out as a result of its exposure to the rapid water flows. This decline in depth continues until the water level in the reservoir is close to the residual dam height (Fig. 7g and h). At this point no further erosion occurs.

3.1.2. Hydrological evolution process of outburst flood

Fig. 8 shows a sample hydrograph of the landslide dam overtopping failure process. The initial time (t_0 = 0 s) is kept along the same timeline with the evolution process of the breach. There is a period during which

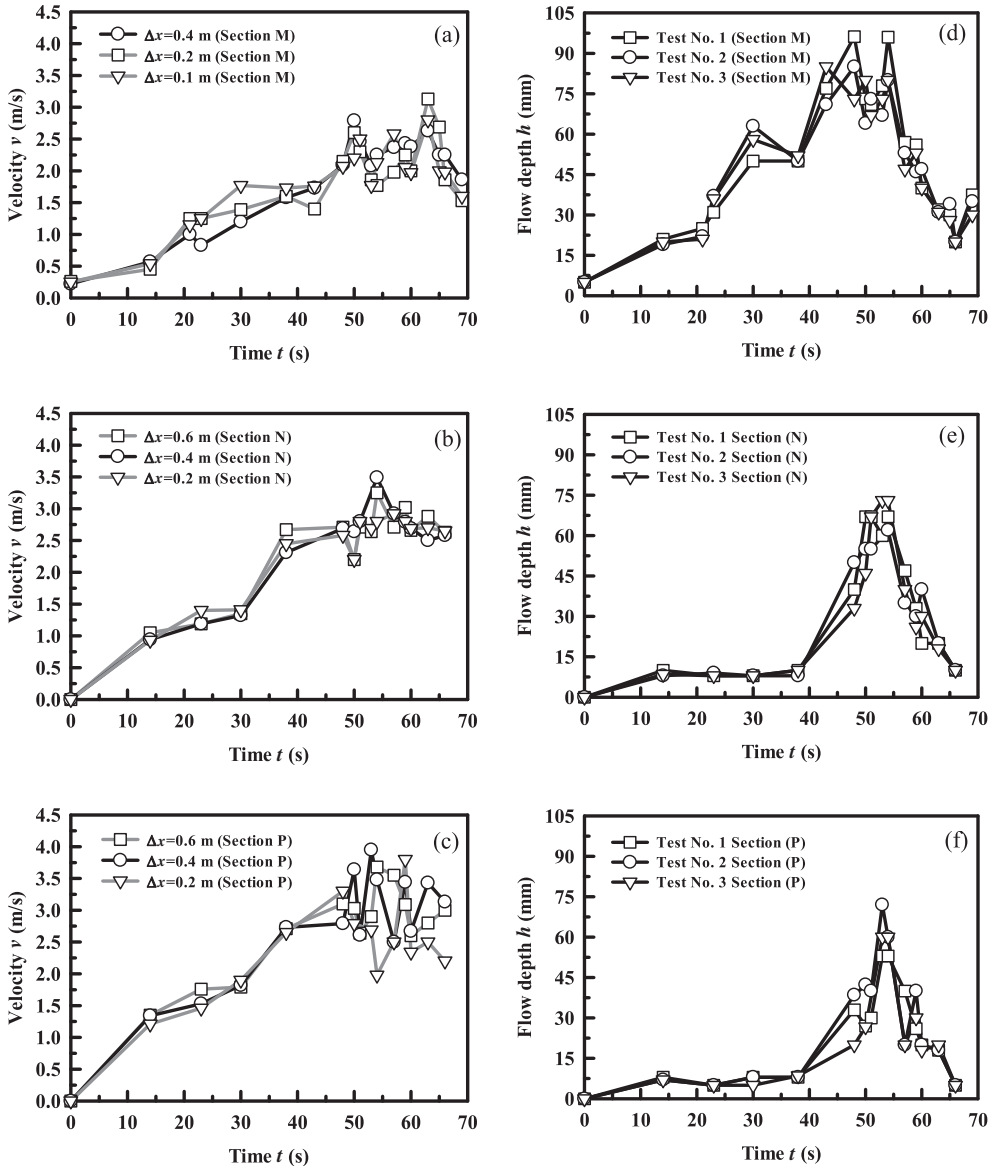

Fig. 6. Flow velocities measured using different spatial windows at cross-sections (a) M, (b) N, and (c) P. Flow depths measured at three different instances at cross-sections (d) M, (e) N, and (f) P.

the outburst flood keeps developing before the front head arrives at the downward measurement location (5 m away from the landslide dam toe), and therefore no measured data exists before $t = 32$ s in Fig. 8a. After that time, the outburst discharge begins to gently increase, marking the arrival of the initial and minor surges. At $t = 47$ s, an inflection point – a sudden positive change in the discharge trend – is observed, marking the occurrence of outburst flooding. This steep rise in the discharge profile ends when the peak discharge is achieved, which is 7 s from the inflection point. Thereafter, the outburst flood attenuates while maintaining a relatively large discharge over a longer period of time compared to the flows before the inflection point. Near the end of the experiment, as the outburst floods weaken, the measured discharges gradually decrease, asymptotically approaching the value $\frac{Q_{out}}{Q_{in}} = 1$. At $t = 80$ s, the erosion stops.

Similar to outburst flood hydrography, determining the flow properties of the induced outburst floods is also necessary for disaster prevention and mitigation. The density of the outburst floods were measured (Fig. 8b). Although the flood density fluctuates in Fig. 8b, the trend shows a steady decrease. During the early stages of the dam failure, the flood density is relatively high, indicating the formation of debris flows (cf. Jiang et al., 2016) (Fig. 8b). The outburst flow is unstable mainly due to the irregular collapses of soils that occur along the longitudinal direction due to head-cut erosion. At the end of the head-cut erosion process, the fluctuation of the flow density eases. The transition to the lower densities corresponds to the time at which the peak discharges were recorded, at around $t = 54$ s. The outburst floods in this stage are mostly low-density turbidity currents according to Middleton and Hampton (1973) and Mulder and Alexander (2001) (with densities lower than 1165 kg/m^3) (Fig. 8b). After $t = 54$ s, the densities of the outburst floods further reduced (Fig. 8b). Erosion stops at the end of the dam failure, and the turbidity currents gradually changes to clear water (same as the upstream inflow) with a density of about 1000 kg/m^3.

Upon comparing the hydrograph in Fig. 8 with the cross-sectional evolution of the overtopping failure in Fig. 7e, one can find that the inflection point (at $t = 47$ s) roughly coincides with the time at which the erosion point reaches the upstream dam crest, whereupon the dam crest was totally eroded (at $t_4 = 43$ s). In addition, there is a coincidence between the amount of erosion observed at $t_5 = 51$ s (Fig. 7f) and the peak discharge of the outburst flood at $t = 54$ s, as measured

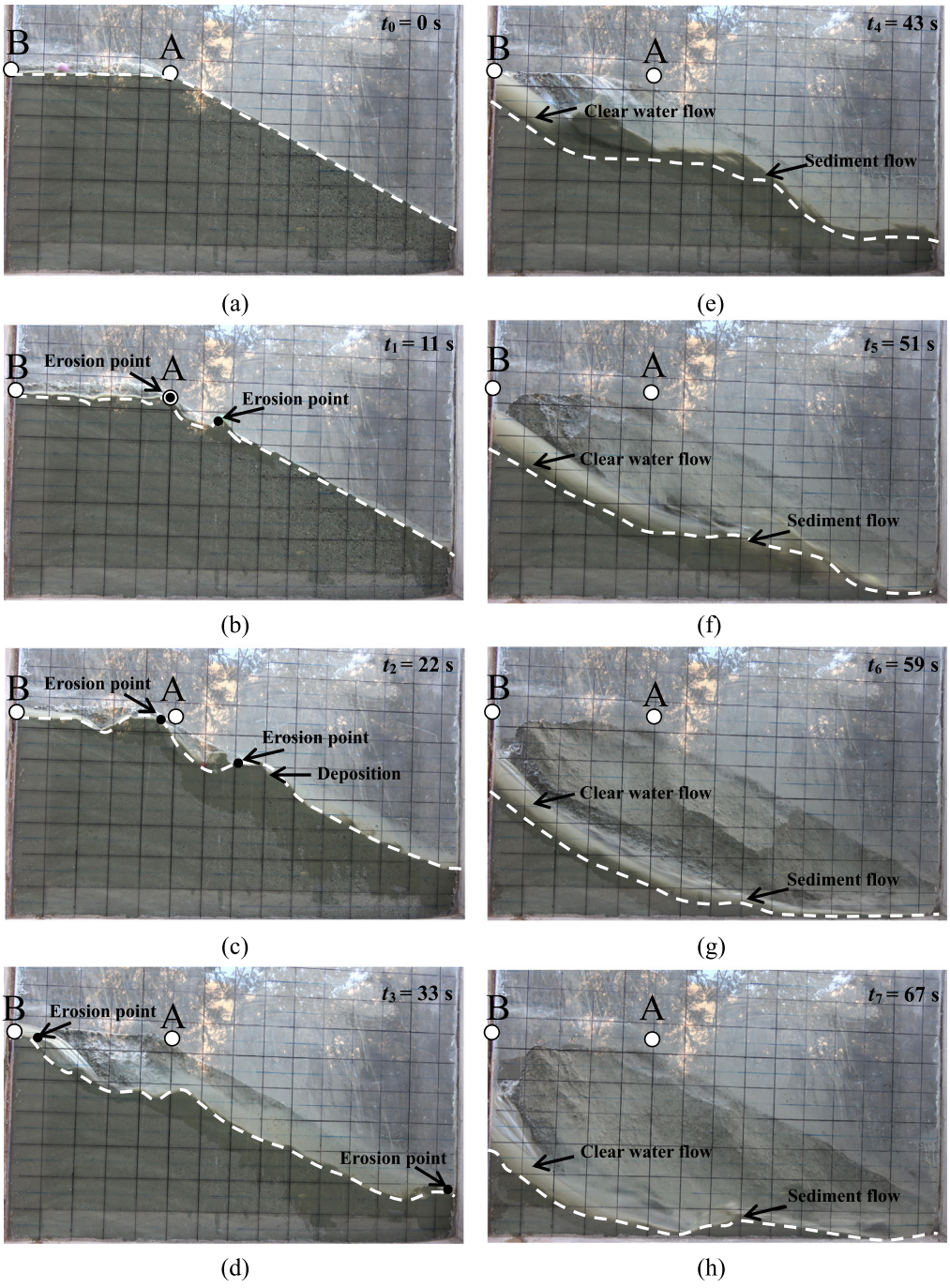

Fig. 7. Longitudinal snapshots of the dam-breaching process (Test No. C-Q5.3). $t_0 = 0$ s is the moment when water starts to travel along the initial notch and eventually reaches the downstream crest. The grid size on the window is 0.1 m × 0.1 m. The dashed lines mark the surface profile of the erodible bed.

downstream (Fig. 8). Note that the minor time difference is because the outburst floods need to flow five meters away from dam toe. This relationship indicates that the inflection point physically corresponds to the point when the dam crest was totally eroded which resulted in outburst flooding. The results can be explained by the broad-crest weir equation proposed by Singh and Scarlatos (1988) and Coleman et al. (1997):

$$Q = CB_w(H-Z)^{3/2} \tag{2}$$

where C is a discharge coefficient, B_w is the width of cross-section, H is the height of reservoir, and Z is the elevation of breach bottom. The equation states that the amount of discharge increases with the increase of the relative height between the water level in the dammed lake and the dam crest (Coleman et al., 1997).

From the hydrograph and longitudinal surface profiles, three distinct stages of dam failure can be defined. The rate of change of the outburst discharge can be used to help explain the three-stage division:

$$\beta = \frac{\Delta Q_i}{\Delta t} \tag{3}$$

where β is the rate of change of outburst discharge, ΔQ_i is the relative dimensionless discharge, and Δt is the change in time. Stage 1 is termed the 'headcut erosion process'. This stage starts when the first erosion point moves from the downstream dam crest at Point A to the upstream

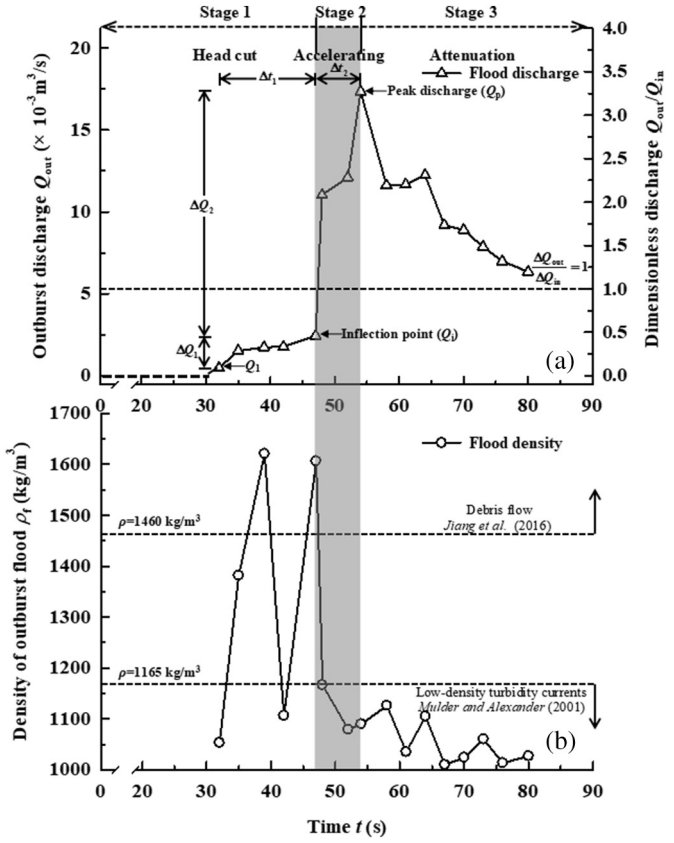

Fig. 8. (a) Hydrograph for dam-breach experiment reported in this paper; (b) the density of outburst floods. Time $t = 0$ s marks the moment when water starts to travel along the initial notch and eventually reaches the downstream crest. Δt_1 is the time between the first recorded outflow discharge to the inflection point. Δt_2 is the relative time from the inflection point to the peak discharge. ΔQ_1 is the dimensionless value between the initial and final discharge prior to the inflection point $\left(\frac{Q_1-Q_1}{Q_{in}}\right)$ while ΔQ_2 is the dimensionless value between peak discharge and the discharge at the inflection point $\left(\frac{Q_p-Q_1}{Q_{in}}\right)$.

dam crest at Point B. The pertinent outburst discharge increases from zero to the inflection discharge. The flow density at this stage is relatively large and can be considered to be hyperconcentrated flows or even debris flows measured downstream of the dam (Fig. 8b). During this stage, both the value of the outburst discharge and the rate of change are small ($\beta_1 = 0.02$). During Stage 2, which can be called as 'accelerated erosional process', the erosion point reaches the upstream dam crest (at Point B), the depth and the downstream velocity of the water flow rapidly increases. This causes the outflow discharge to rapidly increase ($\beta_2 = 0.4$) until the peak discharge is achieved. The densities of the flow in this stage decrease rapidly and can be classified as low-density turbidity currents (Fig. 8b). During Stage 3, called the 'attenuating erosional process', the water flow depth and the outflow discharge starts to decrease, and the landslide dam undergoes rapid failure. Eventually, the outflow discharge equalizes with the value of the upstream inflow $\left(\frac{Q_{out}}{Q_{in}} = 1\right)$. Comparing the rates of change of the outburst flow discharge during Stages 1 (β_1) and 2 (β_2), it can be seen that $\beta_1 \ll \beta_2$ in all tests (see Table 1). This further illustrates that before the water erosion point approaches the upstream crest Point B, the outflow discharge is small $\left(\frac{Q_{out}}{Q_{in}}<1\right)$, and so is the rate of outflow discharge change β. However, once the soil at the upstream dam crest (Point B) has been completely eroded, the discharge rate of outburst flooding will also rapidly increase. Such a clear turning point serves as a good criterion for the identification of the two different stages (Stages 1 and 2), which can be used as a guideline for the providing early warnings for landslide dam failures.

3.2. Influence of upstream inflow discharge on the downstream outburst floods

As shown in Fig. 9, the larger the inflow discharge (Q_{in}), the shorter the time needed to reach the inflection point (Δt_1), and the shorter time required to achieve the peak discharge ($\Delta t_1 + \Delta t_2$). It also follows that the larger the inflow, the larger the peak discharge (Q_p). This linear relationship, as shown in Fig. 9, was found to be quite weak. During Stage 1, the upstream inflow (Q_{in}) mostly serves to supplement the amount of water lost during the initial dam failure due to overtopping. The larger the upstream flow discharge, the higher the water level that will be retained. According to Bernoulli's principle, the outflow velocity is approximately proportional to the square of the water level behind the dam (following conservation of energy) (Chanson, 2004). Consequently, higher flow velocities result in stronger erosion of the dam material. This accelerates the transition of the erosion point from the downstream crest Point A to the upstream crest Point B, effectively reducing the time to the hydrograph inflection point (Δt_1). However, it was observed that Δt_1 no longer changes when the upstream flow discharge is larger than 5.3×10^{-3} m^3/s, which means other factors (e.g., dam material, void ratio) rather than inflow discharges may govern the change of Δt_1 at this time.

3.3. Longitudinal evolution model of landslide dam failure

Fig. 10 shows the profiles of eroded dam surfaces at different moments (Test No. C-Q5.3). At the beginning of Stage 1, due to the weak hydrodynamic power, only the downstream crest Point (A) is eroded. The erosion point then moves towards the upstream crest Point (B) over time. This result fits well with the model of Zhong et al. (2018), which defines the initial erosion as an anticlockwise process, wherein the axis of rotation is at the dam toe (Erosion develops from the downstream dam crest Point A towards the upstream dam crest Point B). However, Fig. 10 illustrates that the rotation point is not fixed at the dam toe during the breaching of the dam. It keeps moving along the downstream dam slope from the crest to the dam toe. In addition, due to the small outflow discharge and velocity at the initial stage (Figs. 6 and 8), the eroded sediments cannot be completely entrained into the downstream flow. They may become deposited, and accumulate on the dam slope (Fig. 10 'area (a)'). This further leads to the irregularity of the surface of the sloping bed in Stage 1 compared to the flat linear surfaces proposed by Chang and Zhang (2010) and Zhong et al. (2018). At Stage 2, the stream power is sufficient for the flow velocity to gradually increase. The irregular longitudinal profiles are quickly flattened by the rapid water and sediment flows. Although irregular curves occasionally appear, the longitudinal profiles of the erodible

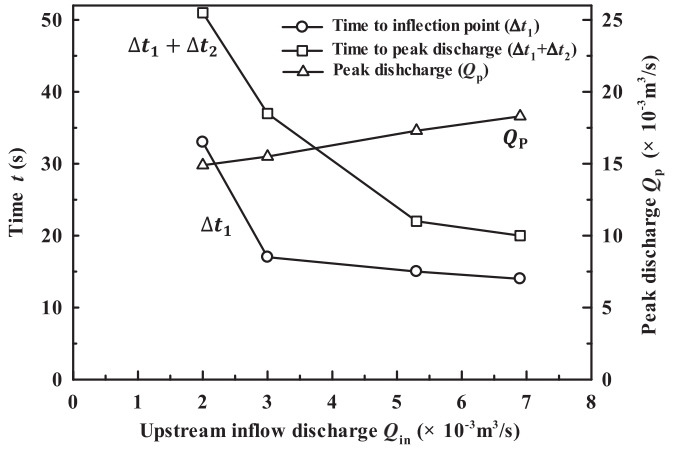

Fig. 9. Influence of upstream flow discharge on the time of Stages 1 and 2 and the pertinent peak flow discharge.

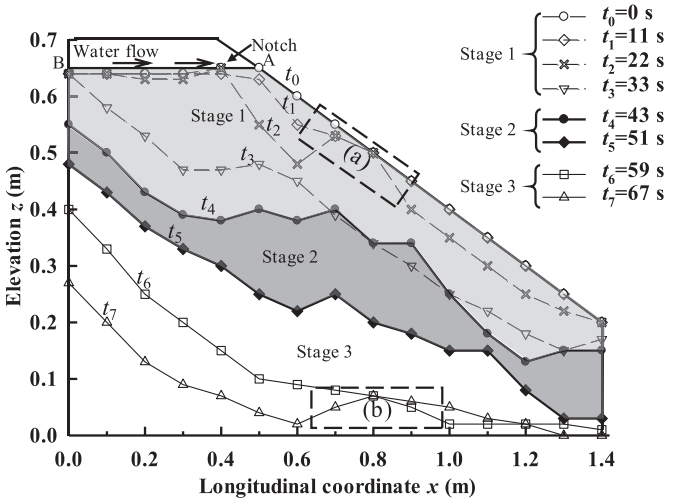

Fig. 10. Longitudinal profiles along breach channel for dam (Test No. C-Q5.3). The different lines with symbols represent the surface profiles at different moments while the shaded regions represent the different stages.

bed are mostly smooth (see Fig. 10). These smooth curves along the flow direction are observed in both Stages 2 and 3. During Stage 3, the stream power of the water flow attenuates and sediment accumulation near the toe is observed (Fig. 10, 'area (b)'). A spindle-like area between two surface profiles is also noted during the rapid erosion stages. This longitudinal evolution process is different from the previous hypothetical model proposed by Chang and Zhang (2010) and Zhong et al. (2018).

Fig. 11 shows the changes in elevation along the longitudinal direction for a time interval of $\Delta t = 1$ s because of the erosion downstream. The solid line represents the initial surface profile of the dam at $t = 54$ s, while the dashed line is the resulting profile after erosion has taken place at $t = 55$ s. At the inset (Fig. 11a), the erosion rate is plotted against their corresponding positions along the said profile at the initial time. Here, a maximum erosion rate E_{max} is measured at 0.8 m, which is near the middle of longitudinal coordinate. As shown in Fig. 11b, the relative erosion rate $\frac{E_i}{E_{max}}$, defined as the erosion rate at a specific point divided by the maximum erosion rate, is super-imposed on the longitudinal profile to further illustrate the erosion process along the flow

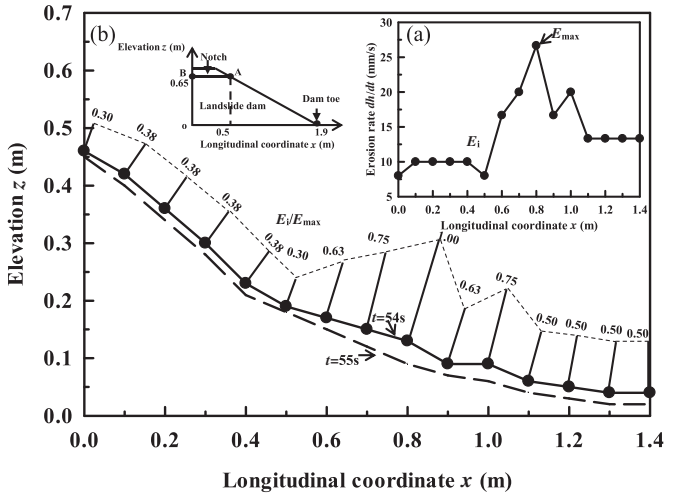

Fig. 11. Infinitesimal analysis for longitudinal evolution at $t = 54$ s (Test No. C-Q5.3). (a) Longitudinal profiles along the left side of the dam, and corresponding erosion rate along the longitudinal direction, (b) the relative erosion rate ($^{E_i}/_{E_{max}}$) along longitudinal direction.

direction. The relative erosion rate is initially steady as it moves downstream. It then starts to rapidly increase at about 0.5 m until it reaches its maximum (unity). After this point the relative erosion rate starts to decrease and levels out at a fixed value as it nears the dam toe. This indicates that the erosion rate first increases and then decreases along the flowing direction on the sloping bed. This erosion rate distribution is also different from the models proposed by Chang and Zhang (2010) and Zhong et al. (2018).

The erosion rates due to landslide dam overtopping failure were studied for different inflow discharges. Different inflow discharges correspond to different rates of erosion at different locations of the dam at different stages of each test (Fig. 12). The erosion rates in Stage 2 are larger than those in Stages 1 and 3 for all values of inflow discharges (2.0×10^{-3}, 3.0×10^{-3}, 5.3×10^{-3}, 6.9×10^{-3} m^3/s). The maximum erosion rate increases with upstream inflow. However, the relative variation of erosion rate along the sloping bed (increasing first and then decreasing), for different values of upstream inflow, are fairly consistent (Fig. 12). Even though there were fluctuations of some of the data points caused by the collapse of the other parts of the dam on the left side of the notch. This shows that the same erosion mechanisms dominate, even at different inflow discharges. In addition, the location of the maximum rate of erosion rate moves away from the downstream part of the crest in Stage 1 (Point A, x = 0.5 m) and towards the dam toe in Stage 2 before once again returning to the region near the downstream part of the crest (Point A) (Fig. 12).

Based on the landslide dam breaching process presented, a new longitudinal evolution model is proposed (Fig. 13). For simplicity, smoothed curves are used to represent the longitudinal profile, disregarding the shape irregularities brought about by local geomorphological changes due to erosion and/or deposition (Fig. 13). a_1, a_2, a_3, represents the trajectory of the erosion point along the downstream slope at different time and b_1, b_2, b_3, along the dam crest respectively. h_{j-1}, h_j, h_{j+1} represents the different erosion depth along the longitudinal direction at the different time steps. The main characteristics of Stage 1 is that the erosion point initially develops at the downstream dam crest Point (A) and then gradually moves upstream, towards dam crest Point (B), and downstream, towards the dam toe. In Stages 2 and 3, a spindle-like erosion process is emphasized along the longitudinal flow direction. This indicates that the erosion rate can approach a maximum value in the middle part of the dam during each time step along the flow direction, rather than in the beginning or end portion of the dam. This is a marked deviation from previous models.

3.4. Erosion equation

The evolution of the landslide dam failure along the flowing direction is a result of bedload erosion. It is directly affected by the shear stress (τ) exerted by the water flow on the sloping bed and the bedload erosion resistance (τ_c). To ease calculations, outburst flood caused by landslide dam failure is assumed to be uniform flow (cf. Chen et al., 2015; Chen and Zhang, 2015; G.G.D Zhou et al., 2015; X.Q. Zhou et al., 2015; Liu and He, 2017; Garciacastellanos and O'Connor, 2018). The bed shear stress can be estimated from the measured hydraulic radius and the measured velocity based on Manning's equation (Wu, 2013; Chen et al., 2015; Chen and Zhang, 2015; G.G.D Zhou et al., 2015; X.Q. Zhou et al., 2015; Zhong et al., 2018):

$$\tau = \frac{\rho_w g n^2 v^2}{R^{1/3}} \tag{4}$$

where ρ_w is the water density (1000 kg/m^3). The outburst flows in rapid erosion Stages 2 and 3 are low-density turbidity currents, therefore, the use of the density of water in the following calculations (for Stages 2 and 3) is a simplifying assumption. This is particularly the case in Section M where no granular material can be transported. g is the acceleration due to gravity, n is the Manning coefficient, v is the velocity of fluid,

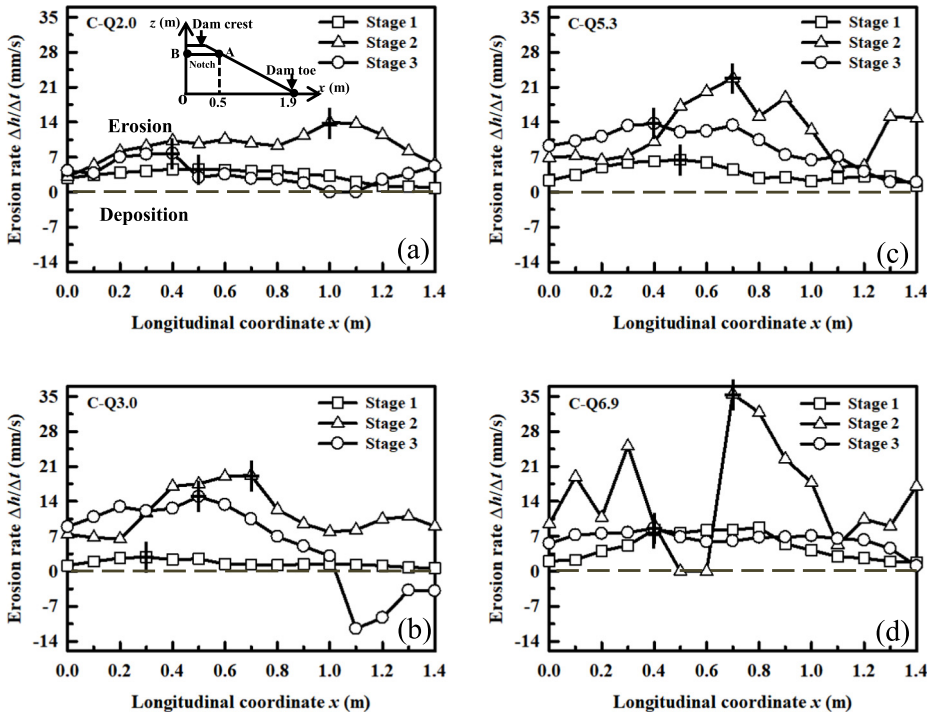

Fig. 12. The change of erosion rate in three stages for the four upstream inflow discharges: (a) $Q_{in} = 2.0 \times 10^{-3}$ m^3/s (b) $Q_{in} = 3.0 \times 10^{-3}$ m^3/s. (c) $Q_{in} = 5.3 \times 10^{-3}$ m^3/s. (d) $Q_{in} = 6.9 \times 10^{-3}$ m^3/s. '+' represents the location of maximum erosion points in three different stages.

and R is the hydraulic radius. The Manning's n value is related to bedload median grain size d_{50} (in meter) (Wu, 2013; Zhong et al., 2018):

$$n = \frac{d_{50}^{1/6}}{A_n} \tag{5}$$

where A_n is an empirical coefficient. Modeling tests show that $A_n = 16$ for laboratory scale and 12 for field scale (Wu, 2013). The hydraulic radius, considering side-wall effects in shallow flows where the depth of the water is less than half of the width of the cross-section ($h<b/2$), is calculated using the relationship proposed by Vanoni and Brooks (1957):

$$R = \frac{h(b-h)}{b} \tag{6}$$

It is assumed that b is higher than h, and so $R = h$ can be adopted (cf. Guo and Jin, 1999; Liu and He, 2017).

To find the relationship between the rate of erosion and shear stress, we once again refer to the dam cross-sections 'M', 'N' and 'P'. The erosion rate E and shear stresses τ at cross-section M were measured and calculated at Stages 1, 2 and 3. They were then plotted against each other. Linear relationships between E and τ were observed during the last two Stages (Fig. 14a), and can be defined according to the equation:

$$E = k_d(\tau - \tau_c) \tag{7}$$

where k_d is the erodibility of soil and depends on the lithology of the material (Garciacastellanos and O'Connor, 2018). For comparison, the relationship between the rate of erosion and the shear stress for a field case, specifically the Tangjiashan landslide dam failure (cf. Chen et al., 2015; G.G.D Zhou et al., 2015; X.Q. Zhou et al., 2015), was also analyzed in this study. Different from well-controlled physical modeling tests, it is difficult to identify the exact time when the erosion point arrived at the upstream crest (Stage 1). However, a sudden drop in the recorded water level was recorded by an automatic hydro-gauge station, followed by outburst flooding. Thus, the rapid erosion stage (Stages 2 and 3) can be determined. It was recorded to have started at 9:30 a.m. on 10 June 2008 and ended at 3:00 p.m. on 10 June 2008. The end was defined as the time when the erosion rate was close to zero or even negative. A linear relationship between the bed erosion rate E and the shear stress τ for the Tangjiashan landslide dam in the rapid erosion stages

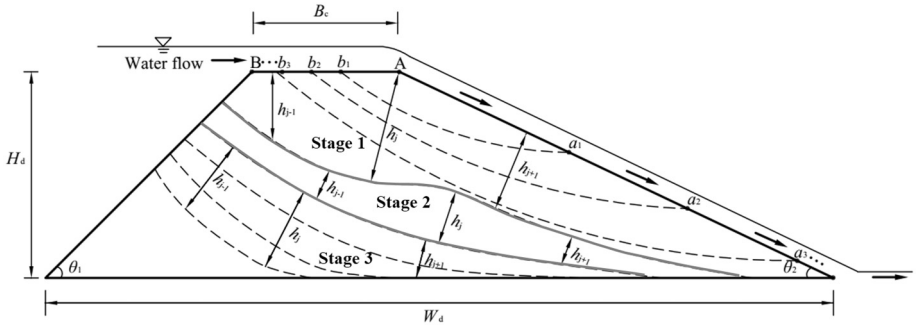

Fig. 13. Proposed the evolution of longitudinal breach profile of the landslide dam based on our test, h_j is the maximum erosion height of a certain stage, and h_{j-1}, h_{j+1} are the erosion height of randomly chosen point before and after the maximum erosion height point, respectively.

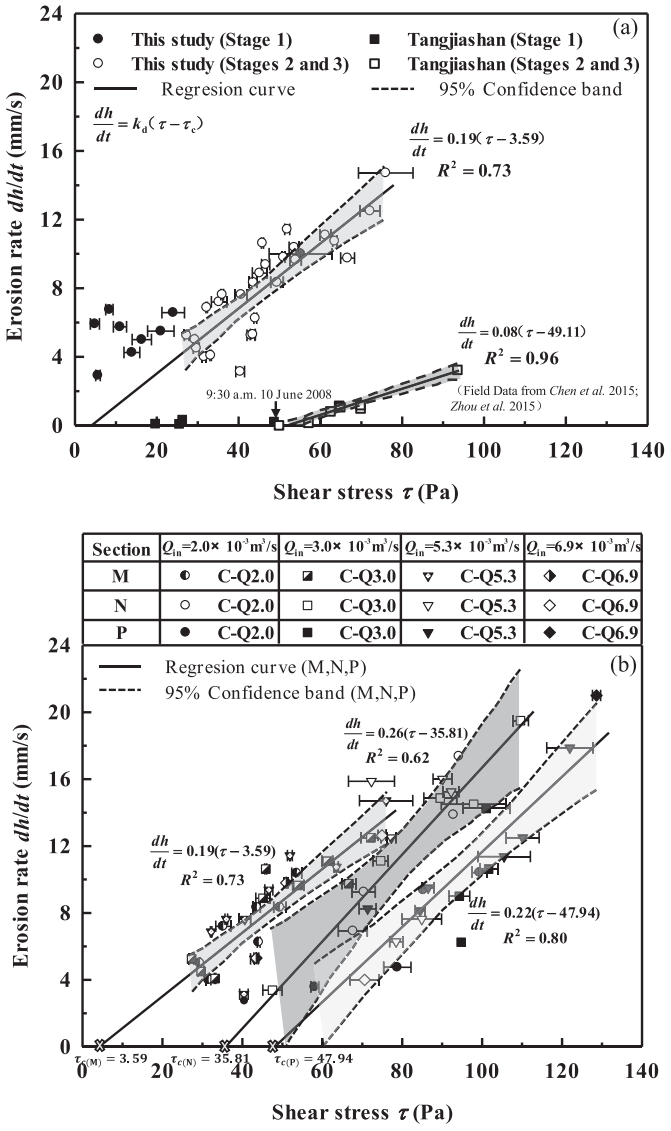

Fig. 14. (a) A representative (Section M) relationship between erosion rate and shear stress obtained from the experiments and from the Tangjiashan landslide dam (cf. Chen et al., 2015; G.G.D Zhou et al., 2015; X.Q. Zhou et al., 2015). (b) The relationship between erosion rate and shear stress at the different sections (M, N, P) for all experiment set-up during Stages 2 and 3. Error bars for shear stress express standard deviations of distributed measurements, and linear line, R^2 values summarize results of regression analysis. The shadows are based on a 95% confidence interval.

also can be found (Fig. 14a). Like the modeling tests, the data points of the slow erosion stage (Stage 1) do not follow this relationship. Actually, due to the simplicity of this linear relationship, it has already been widely used in the numerical simulations (e.g., Chang and Zhang, 2010; Wu, 2013; Zhong et al., 2018) to study the landslide dams overtopping failure. Based on this experimental study, the linear relationship between erosion rate and shear stress has been further verified. However, what should be noted is that this linear relationship is only applicable for the rapid erosion stages (Stages 2 and 3) and not for the headcut erosion stage (Stage 1).

Over the past decades, extensive efforts have been made to predict the resistance of soil to erosion. Some of the existing empirical equations (which are widely used in defining erosion resistance in dam failures) are summarized in Table 2. The empirical formulas imply that the erosion resistance depends only on particle/void sizes (d_{50}, P_C, P) and density (e, $\rho_{d,}$ ρ_b) of the granular materials. Once the granular particles of the landslide dams are well mixed and uniformly distributed inside the dam body like the physical modeling tests in this study, the erosion resistance should keep the same value everywhere and remain unchanged during the dam failure.

To test this hypothesis, the experimental results about the erosion rate-shear stress relationships during Stages 2 and 3 at Sections M, N, and P are interpreted. All the points in these three sections fall into three independent intervals (95% confidence interval), which implies the independence of the processes at each section with each other. By linear fitting the points at different sections, three approximately parallel lines (Fig. 14b) show that k_d (slope of lines) is almost the same within the dam body, while the erosion resistance (τ_c) (the intercept of the three lines on the abscissa) increases along the direction of the flow. The relative invariance of the erodibility of soils k_d throughout the dam body is thought to be due to the well-controlled conditions (i.e. void ratio, soil densities) at which it was constructed (Garciacastellanos and O'Connor, 2018). Furthermore, quantitative comparisons have been made by comparing the calculated results based on the empirical equations in Table 2 with the modeling test results. The erosion resistance of the dam body against clear water flows that developed mostly in position M ($\tau_{c(M)}$ =3.59 Pa) (Fig. 14b) is very close to the values calculated from Table 2, which covers the values $0.49 \le \tau_c \le 7.70$ Pa. However, the erosion resistance of the dam body against sediment flows that were measured in positions N and P, $\tau_{c(N)}$ =35.81 Pa and $\tau_{c(P)}$ =47.94 Pa respectively, are far beyond the calculated range (Fig. 14b). One possible reason for the increased apparent erosion resistance along the downstream direction is the decreased capacity of the flowing water to entrain sediment because the sediment concentration (C_s) is already higher than that upstream (cf. Wang and Xu, 1998). Thus the 'apparent' erosion resistance of the bedload on the sloping bed is then not only a function of erodible soil strength but

Table 2
Empirical equations for calculation of the shear resistance (τ_c).

Empirical expression	Calculated τ_c in this study (Pa)	Main parameters	References
$\tau_c = 3.54 \times 10^{-28.1 d_{50}}$	3.35	d_{50}: mean particle size (m)	Smerdon and Beasley (1961)
$\tau_c = 0.16(PI)^{0.84}$	~	PI: plastic index (%)	
$\tau_c = 0.493 \times 10^{0.0182 P_c}$	0.54	P_c: percent of clay by weight (%)	
$\tau_c = 10.2(D_r)^{-0.63}$	~	D_r: dispersion ratio	
$\tau_c = 0.0012{\rho_d}^{1.2}$	7.70	ρ_d: dry density (kg/m^3)	Ockenden and Delo (1988)
$\tau_c = \xi(\rho_b - 1)$	0.49	ξ: coefficient	Mehta (1988)
		ρ_b: bulk density of soil (kg/m^3)	
$\tau_c = 0.015(\rho_b - 1000)^{0.73}$	1.38	ρ_b: bulk density of soil (kg/m^3)	Mitchener and Torfs (1996)
$\tau_c = \tau_0\left(\frac{H_p}{H_e}\right)^2$	~	τ_0: maximum shear stress (Pa)	Hanson and Cook (1997) and Hanson and Simon (2001)
		H_p:potential core length (m)	
		H_e: distance from the jet nozzle (m)	
$\tau_c = 5.44 \times 10^{-4}\rho_b - 0.28$	0.53	ρ_b: bulk density of soil (kg/m^3)	Amos et al. (2004)
$\tau_c = 0.1 + 0.1779P + 0.0028P^2 - 2.34 \times 10^{-5}P^3$	2.70	P: fines content (%)	Julian and Torres (2006)
$\tau_c = \frac{2}{3}gd(\rho_s - \rho_w)\tan\varphi$	5.29	ρ_w: mass density of water (kg/m^3)	Annandale (2006)
		ρ_s: unit weight of soil (kg/m^3)	
		φ: friction angle	
$\tau_c = 6.8(PI)^{1.68}P^{-1.73}e^{-0.97}$	~	e: void ratio	Chang et al. (2011)

also of sediment concentration of flow above. This indicates that in the longitudinal direction, the erosion rate of the landslide dam does not necessarily increase due to the flow capacity; the evolution is spindle-shaped instead. This is despite the continued increase of the shear stress provided by the water flow. If our interpretation of this finding is correct, the relationship between erosion rate and shear stress needs to be adjusted when incorporating it to physically-based breach models.

4. Conclusions

By using flume modeling tests, the longitudinal evolution process of landslide dam failure due to overtopping and the effects of the upstream inflow on outburst flooding were investigated. The key conclusions are:

1. According to the hydrographs of downstream outburst floods, three stages of dam breach evolution can be identified. Once the upstream dam crest is eroded by the water flow, an inflection occurs in the hydrograph, marking the occurrence of an outburst discharge. The outflow discharge then rapidly increases until a peak is achieved. Such criterion provides an appropriate indicator for providing early warnings of landslide dam disasters. The larger the inflow, the shorter the time it takes to reach the inflection discharges, and the shorter the time to it takes to reach the peak discharge. In addition, the dependence of peak discharge on inflow discharge is relatively weak.
2. A new longitudinal evolution model is proposed in this study to capture the features of the three different stages. Stage 1 is characterized by the movement of the erosion point from the downstream dam crest to the direction of the upstream dam crest and to the dam toe. In Stages 2 and 3, a spindle-like erosion is observed along the flow direction, indicating that the erosion rate initially increases and then decreases along the water flow direction.
3. The longitudinal evolution of the dam failure along the flow direction is a result of bedload erosion. A linear equation $E = k_d(\tau - \tau_c)$ defines the relationship between erosion rate and shear stress in dam-breaching process (Stages 2 and 3), which is also applicable to the Tangjiashan landslide dam failure process. In addition, when taking different positions into consideration, different 'apparent' erosion resistances (τ_c) are observed in the dam breaching experiments. It increases along the flow direction. The relationship between the erosion rate and shear stress needs to be adjusted when incorporating it in physically-based breach models.

The failure process of a landslide dam is a complicated process which involves geotechnical and hydro-dynamic concepts. As a simplification, the void ratio of the dam is kept large and uniform along the depth in this experiment to conform to the characteristics of naturally loose accumulation. The situation where the normal stress results in an uneven distribution of porosity after a long period of consolidation is not considered in this paper. This will be the focus of our future work, along with the consideration of the interactions between the soil resistance and water shear stress during the landslide dam failure.

Notations

A	the intersection point of dam crest and downstream dam slope
A_n	empirical coefficient in Manning parameter
a	empirical coefficient in erosion equation
a_1, a_2, a_3,	the trajectory of the erosion point along the downstream slope
B	the intersection point of dam crest and upstream dam slope
B_w	width of cross-section
B_c	width of dam crest
b	empirical coefficient in erosion equation
b_0	width of cross-section
b_1, b_2, b_3,	the trajectory of the erosion point along the dam crest
C	discharge coefficient
C_s	concentration of solid
D_r	dispersion ratio
d_{16}, d_{50}, d_{84}	grain sizes; subscript indicates percent smaller
E	erosion rate expressed as thickness per unit time
e	void ratio
g	acceleration due to gravity
H	height of the water level in dammed lake
H_d	height of landslide dam
H_e	distance from jet nozzle
H_p	potential core length
h_0	height of notch
h	the depth of water
h_j	the erosion depth
k_d	erodibility of solid
L	tracer particle travel distance
L_0	the length of downstream slope
n	Manning coefficient
P	fine content
P_c	percent of clay by weight
PI	plastic index
Q_{in}	the upstream inflow discharge
Q_{out}	the outburst flood discharge
Q_p	peak discharge
R	hydraulic radius
t	time
V_l	volume of dammed lake
V_d	volume of landslide dam
v	velocity of fluid
w_0	width of notch
W_d	width of landslide dam
Z	the elevation of breach bottom
a	flume inclination angle
β	rate of change of outburst discharge
β_1, β_2	rate of change of outburst discharge in Stage 1, Stage 2 respectively
σ_g	d_{84}/d_{16} dimensionless measure of the spread in the grain-size
θ_1	angle of upstream dam toe
θ_2	angle of downstream dam toe
ΔQ_i	relative dimensionless discharge
Δx	tracer particle travel distance in horizontal direction
Δy	tracer particle travel distance in vertical direction
ξ	coefficient in calculate erosion resistance
ρ_b	bulk density of soil
ρ_d	dry density
ρ_f	outburst flood density
ρ_s	unit weight of solid material
ρ_w	density of water
τ	shear stress exerted by water flow
τ_0	maximum shear stress
τ_c	sediment erosion resistance
φ	friction angle of solid

Acknowledgments

The authors acknowledge the financial support from the National Natural Science Foundation of China (grant Nos. 41731283, 11672318), the Key Research Program of Frontier Sciences, Chinese Academy of Sciences (CAS) (grant no. QYZDB-SSW-DQC010), and the Chinese Academy of Sciences (CAS) Pioneer Hundred Talents Program.

References

Amos, C.L., Bergamasco, A., Umgiesser, G., Cappucci, S., Cloutier, D., Denat, L., Flindt, M., Bonardi, M., Cristante, S., 2004. The stability of tidal flats in Venice Lagoon—the results of in-situ measurements using two benthic, annular flumes. J. Mar. Syst. 51 (1), 211–241. https://doi.org/10.1016/j.jmarsys.2004.05.013.

Annandale, G.W., 2006. Scour technology: mechanics and engineering practice. McGraw-Hill, New York 430. https://doi.org/10.1036/0071440577.

Baba, H.O., Peth, S., 2012. Large scale soil box test to investigate soil deformation and creep movement on slopes by Particle image Velocimetry (PIV). Soil Tillage Res. 125, 38–43. https://doi.org/10.1016/j.still.2012.05.021.

Cao, Z., 1999. Equilibrium near-bed concentration of suspended sediment. J. Hydraul. Eng. 125 (12), 1270–1278. https://doi.org/10.1061/(asce)0733-9429(1999)125:12(1270.

Cao, Z., Yue, Z., Pender, G., 2011. Landslide dam failure and flood hydraulics. Part I: experimental investigation. Nat. Hazards 59 (2), 1003–1019. https://doi.org/10.1007/s11069-011-9814-8.

Carrivick, J.L., 2010. Dam break - outburst flood propagation and transient hydraulics: a geosciences perspective. J. Hydrol. 380 (3–4), 338–355. https://doi.org/10.1016/j.jhydrol.2009.11.009.

Casagli, N., Ermini, L., Rosati, G., 2003. Determining grain size distribution of material composing landslide dams in the Northern Apennine: sampling and processing methods. Eng. Geol. 69 (1), 83–97. https://doi.org/10.1016/s0013-7952(02)00249-1.

Chang, D.S., Zhang, L.M., 2010. Simulation of the erosion process of landslide dams due to overtopping considering variations in soil erodibility along depth. Nat. Hazards Earth Syst. Sci. 10 (4), 933–946. https://doi.org/10.5194/nhess-10-933-2010.

Chang, D.S., Zhang, L.M., Xu, Y., Huang, R.Q., 2011. Field testing of erodibility of two landslide dams triggered by the 12 May wenchuan earthquake. Landslides 8 (3), 321–332. https://doi.org/10.1007/s10346-011-0256.

Chanson, H., 2004. The Hydraulics of Open Channel Flow: An Introduction, 2nd ed., 585. Butterworth-Heinemann, Oxford.

Chen, H.X., Zhang, L.M., 2015. EDDA 1.0: intergrated simulation of debris flow erosion, deposition and property changes. Geosci. Model Dev. 8 (3), 829–844. https://doi.org/10.5194/gmd-8-829-2015.

Chen, Z., Ma, L., Yu, S., Chen, S., Zhou, X., Sun, P., Li, X., 2015. Back Analysis of the Draining Process of the Tangjiashan Barrier Lake. J. Hydraul. Eng. 141 (4), 05014011. https://doi.org/10.1061/(asce)hy.1943-7900.0000965.

Coleman, S.E., Jack, R.C., Melville, B.W., 1997. Overtopping breaching of noncohesive embankment dams. Proc., 27th Congress of the Int. Association for Hydraulic Research, San Francisco.

Coleman, S.E., Andrews, D.P., Webby, M.G., 2002. Overtopping Breaching of Noncohesive Homogeneous Embankments. J. Hydraul. Eng. 128 (9), 829–838. https://doi.org/10.1061/(asce)0733-9429(2002)128:9(829).

Costa, J.E., Schuster, R.L., 1988. The formation and failure of natural dam. Geol. Soc. Am. Bull. 100, 1054–1068.

Cristofano, E.A., 1965. Method of Computing Erosion Rate of Failure of Earth Dams. U.S. Department of the Interior, Bureau of Reclamation, Denver.

Cui, P., Zhou, G.G.D., Zhu, X.H., Zhang, J.Q., 2013. Scale amplification of natural debris flows caused by cascading landslide dam failures. Geomorphology 182 (427), 173–189. https://doi.org/10.1016/j.geomorph.2012.11.009.

Fread, D.L., 1988. BREACH: an erosion model for earthen dam failures. National Weather Service. Office of Hydrology Silver Spring, MD.

Garciacastellanos, D., O'Connor, J.E., 2018. Outburst floods provide erodability estimates consistent with long-term landscape evolution. Sci. Rep. 8 (1). https://doi.org/10.1038/s41598-018-28981-y.

Gaucher, J., Marche, C., Mahdi, T.F., 2010. Experimental investigation of the hydraulic erosion of noncohesive compacted soils. J. Hydraul. Eng. 136 (11), 901–913. https://doi.org/10.1061/(asce)hy.1943-7900.0000274.

Gregoretti, C., Maltauro, A., Lanzoni, S., 2010. Laboratory experiments on the failure of coarse homogeneous sediment natural dams on a sloping bed. J. Hydraul. Eng. 136 (11), 868–879. https://doi.org/10.1061/(asce)hy.1943-7900.0000259.

Guo, Q.C., Jin, Y.C., 1999. Modeling sediment transport using depth-averaged and moment equations. J. Hydraul. Eng. 125 (12), 1262–1269. https://doi.org/10.1061/(asce)0733-9429(1999)125:12(1262.

Hakimzadeh, H., Nourani, V., Amini, A.B., 2014. Genetic programming simulation of dam breach hydrograph and peak outflow discharge. J. Hydrol. Eng. 19 (4), 757–768. https://doi.org/10.1061/(asce)he.1943-5584.0000849.

Hanson, G.J., Cook, K.R., 1997. "Development of excess shear stress parameters for circular jet testing." American Society of Agricultural Engineers Paper 972227, ASAE, St. Joseph, MI.

Hanson, G.J., Simon, A., 2001. Erodibility of cohesive streambeds in the loess area of the midwestern USA. Hydrol. Process. 15 (1), 23–38. https://doi.org/10.1002/hyp.149.

Hanson, G.J., Cook, K.R., Hunt, S.L., 2005. Physical modeling of overtopping erosion and breach formation of cohesive embankments. Trans. ASAE 48 (5), 1783–1794. https://doi.org/10.13031/2013.20012.

Huang, R., 2009. Some catastrophic landslides since the twentieth century in the southwest of China. Landslides 6 (1), 69–81. https://doi.org/10.1007/s10346-009-0142-y.

Hunt, S.L., Hanson, G.J., Cook, K.R., Kadavy, K.C., 2005. Breach widening observations from earthen embankment tests. Trans. ASAE 48 (3), 1115–1120. https://doi.org/10.13031/2013.18521.

Itoh, T., Ikeda, A., Nagayama, T., Mizuyama, T., 2018. Hydraulic model tests for propagation of flow and sediment in floods due to breaking of a natural landslide dam during a mountainous torrent. Int. J. Sediment Res. 33 (2), 107–116. https://doi.org/10.1016/j.ijsrc.2017.10.001.

Iverson, R.M., 2015. Scaling and design of landslide and debris-flow experiments. Geomorphology 244, 9–20. https://doi.org/10.1016/j.geomorph.2015.02.033.

Jiang, X., Cui, P., Chen, H., Guo, Y.Y., 2016. Formation conditions of outburst debris flow triggered by overtopped natural dam failure. Landslides 14 (3), 821–831. https://doi.org/10.1007/s10346-016-0751-1.

Jiang, X., Wei, Y., Wu, L., Lei, Y., 2018. Experimental investigation of failure modes and breaching characteristics of natural dams. Geomat. Nat. Haz. Risk 9 (1), 33–48. https://doi.org/10.1080/19475705.2017.1407367.

Julian, J.P., Torres, R., 2006. Hydraulic erosion of cohesive riverbanks. Geomorphology 76 (1–2), 193–206. https://doi.org/10.1016/j.geomorph.2005.11.003.

Julien, P.Y., 1995. Erosion and Sedimentation. Combridge University Press, Combridge, U.K.

King, J., Loveday, I., Schuster, R.L., 1989. The 1985 Bairaman landslide dam and resulting debris flow, Papua New Guinea. Q. J. Eng. Geol. Hydrogeol. 22 (4), 257–270. https://doi.org/10.1144/gsl.qjeg.1989.022.04.02.

Korup, O., 2004. Geomorphometric characteristics of New Zealand landslide dams. Eng. Geol. 73 (1–2), 13–35. https://doi.org/10.1016/j.enggeo.2003.11.003.

Korup, O., 2006. Rock-slope failure and the river long profile. Geology 34 (1), 45–48. https://doi.org/10.1130/g21959.1.

Korup, O., Montgomery, D.R., Hewitt, K., 2010. Glacier and landslide feedbacks to topographic relief in the Himalayan syntaxes. Proc. Natl. Acad. Sci. U. S. A. 107 (12), 5317–5322. https://doi.org/10.1073/pnas.0907531107.

Liu, W., He, S., 2017. Dynamic simulation of a mountain disaster chain: landslides, barrier lakes, and outburst floods. Nat. Hazards 90 (2), 757–775. https://doi.org/10.1007/s11069-017-3073-2.

Liu, N., Zhang, J.X., Lin, W., Cheng, W.Y., Chen, Z.Y., 2009. Draining Tangjiashan barrier lake after Wenchuan earthquake and the flood propagation after the dam break. Sci. China, Ser. E: Technol. Sci. 52 (4), 801–809. https://doi.org/10.1007/s11431-009-0118-0.

Liu, J., Zhou, X.C., Chen, W., Hong, X., 2018. Breach discharge estimates and surface velocity measurements for an Earth dam failure process due to overtopping based on the LS-PIV method. Arab. J. Sci. Eng. https://doi.org/10.1007/s13369-018-3310-3.

Liu, W., Hu, K., Carling, P.A., Lai, Z., Cheng, T., Xu, Y., 2018. The establishment and influence of Baimakou paleo-dam in an upstream reach of the Yangtze River, southeastern margin of the Tibetan Plateau. Geomorphology 321, 167–173. https://doi.org/10.1016/j.geomorph.2018.08.028.

Malvern Instruments Ltd (2007) MAN0384-1.0 Mastersizer 2000 User Manual.

Mehta, A.J., 1988. Laboratory Studies on Cohesive Sediment Deposition and Erosion. Physical Processes in Estuaries. Springer Berlin Heidelberg, pp. 427–445.

Middleton, G.V., Hampton, M.A., 1973. Sediment gravity flows: mechanics of flow and deposition. In: Turbidity and Deep Water Sedimentation (Eds G.V. Middleton and A.H. Bouma), SEPM, Pacific Section, Short Course Lecture. Notes 1–38.

Mitchener, H., Torfs, H., 1996. Erosion of mud/sand mixtures. Coast. Eng. 29 (1–2), 1–25.

Mulder, T., Alexander, J., 2001. The physical character of subaqueous sedimentary density flow and their deposits. Sedimentology 48 (2), 269–299. https://doi.org/10.1046/j.1365-3091.2001.00360.x.

Ning, L., Chen, Z., Zhang, J.X., Wei, L., Chen, W., Xu, W.J., 2010. Draining the Tangjiashan barrier lake. J. Hydraul. Eng. 136 (11), 914–923. https://doi.org/10.1061/(asce)hy.1943-7900.0000241.

Ockenden, M.C., Delo, E., 1988. Consolidation and erosion of estuarine mud and sand mixtures - an experimental study. HR Wallingford, Report No. SR 149.

Peng, M., Zhang, L.M., 2012. Breaching parameters of landslide dams. Landslides 9 (1), 13–31. https://doi.org/10.1007/s10346-011-0271-y.

Pickert, G., Weitbrecht, V., Bieberstein, A., 2011. Breaching of overtopped river embankments controlled by apparent cohesion. J. Hydraul. Res. 49 (2), 143–156. https://doi.org/10.1080/00221686.2011.552468.

Powledge, G.R., Ralston, D.C., Miller, P., Chen, Y.H., Clopper, P.E., Temple, D.M., 1989. Mechanics of overflow erosion on embankments. II: hydraulic and design considerations. J. Hydraul. Eng. 115 (8), 1056–1075. https://doi.org/10.1061/(asce)0733-9429(1989)115:8(1056.

Rifai, I., Erpicum, S., Archambeau, P., Violeau, D., Pirotton, M., El Kadi Abderrezzak, K., Dewals, B., 2017. Overtopping induced failure of noncohesive, homogeneous fluvial dikes. Water Resour. Res. 53 (4), 3373–3386. https://doi.org/10.1002/2016wr020053.

Roberts, J., Jepsen, R., Gotthard, D., Lick, W., 1998. Effects of particle size and bulk density on erosion of quartz particles. J. Hydraul. Eng. 124 (12), 1261–1267. https://doi.org/10.1061/(asce)0733-9429(1998)124:12(1261).

Shang, Y., Yang, Z., Li, L., Liu, D., Liao, Q., Wang, Y., 2003. A super-large landslide in Tibet in 2000: background, occurrence, disaster, and origin. Geomorphology 54 (3–4), 225–243. https://doi.org/10.1016/s0169-555x(02)00358-6.

Shields, I.A., 1936. Anwendung der Aehnlichkeitsmechanik and der Turbulenzforschung auf die Geschiebebewegung, Mitt. Preuss. Versuchsanst. Wasserbau Schiffbau 26, Tech. Univ. Berlin, Berlin.

Singh, V.P., Scarlatos, P.D., 1988. Analysis of gradual earth-dam failure. J. Hydraul. Eng. 114 (1), 21–42. https://doi.org/10.1061/(asce)0733-9429(1988)114:1(21).

Smerdon, E.T., Beasley, R.P., 1961. Critical tractive forces in cohesive soils. Agric. Eng. 42 (1), 26–29.

Swanson, F.J., Oyagi, N., Tominaga, M., 1986. Landslide dam in Japan. In: Schuster, R.L. (Ed.), Landslide Dam: Processes Risk and Mitigation. 3, pp. 131–145 American Society of Civil Engineers Geotechnical Special Publication.

van Gorp, W., Schoorl, J.M., Temme, A.J.A.M., Reimann, T., Wijbrans, J.R., Maddy, D., Demir, T., Veldkamp, T., 2016. Catchment response to lava damming: integrating field observation, geochronology and landscape evolution modelling. Earth Surf. Process. Landf. 41 (11), 1629–1644. https://doi.org/10.1002/esp.3981.

Vanoni, V.A., Brooks, N.H., 1957. Laboratory Studies of the Roughness and Suspended Load of Alluvial Streams (California Institute of Technology).

Visser, P.J., 1998. Breach Growth in Sand-Dikes. Communications on Hydraulic and Geotechnical Engineering Report No. 98-1. Delft University of Technology, Netherlands.

Walder, J.S., 2016. Dimensionless erosion laws for cohesive sediment. J. Hydraul. Eng. 142 (2), 04015047. https://doi.org/10.1061/(asce)hy.1943-7900.0001068.

Walder, J.S., Iverson, R.M., Godt, J.W., Logan, M., Solovitz, S.A., 2015. Controls on the breach geometry and flood hydrograph during overtopping of noncohesive earthen dams. Water Resour. Res. 51 (8), 6701–6724. https://doi.org/10.1002/2014wr016620.

Walsh, L.S., Martin, A.J., Ojha, T.P., Fedenczuk, T., 2012. Correlations of fluvial knickzones with landslide dams, lithologic contacts, and faults in the southwestern Annapurna

Range, central Nepalese Himalaya. J. Geophys. Res. 117 (F1). https://doi.org/10.1029/2011JF001984.
Wang, Z., Xu, Y., 1998. A study on channel scour rate of sediment laden flow and river bed inertia. J. Sediment. Res. 2 (1), 1–9.
Wang, F., Dai, Z., Okeke, C.A.U., Mitani, Y., Yang, H., 2018. Experimental study to identify premonitory factors of landslide dam failures. Eng. Geol. 232, 123–134. https://doi.org/10.1016/j.enggeo.2017.11.020.
Wu, W.M., 2013. Simplified physically based model of earthen embankment breaching. J. Hydraul. Eng. 139 (8), 837–851. https://doi.org/10.1061/(asce)hy.1943-7900.0000741.
Wu, S., Yu, M., Wei, H., Liang, Y., Zeng, J., 2018. Non-symmetrical levee breaching processes in a channel bend due to overtopping. Int. J. Sediment Res. 33 (2), 208–215. https://doi.org/10.1016/j.ijsrc.2017.09.007.
Xu, Q., Fan, X.M., Huang, R.Q., Westen, C.V., 2009. Landslide dams triggered by the Wenchuan earthquake, Sichuan province, Southwest China. Bull. Eng. Geol. Environ. 68 (3), 373–386. https://doi.org/10.1007/s10064-009-0214-1.
Yalin, M.S., 1977. Mechanics of Sediment Transport. Pergamon Press, Oxford.
Yin, Y., Wang, F., Sun, P., 2009. Landslide hazards triggered by the 2008 Wenchuan earthquake, Sichuan, China. Landslides 6 (2), 139–152. https://doi.org/10.1007/s10346-009-0148-5.
Zhong, Q.M., Chen, S.S., Mei, S.A., Cao, W., 2018. Numerical simulation of landslide dam breaching due to overtopping. Landslides 15 (6), 1183–1192. https://doi.org/10.1007/s10346-017-0935-3.
Zhou, G.G.D., Ng, C.W.W., 2010. Dimensional analysis of natural debris flows. Revue Canadienne De Géotechnique 47 (7), 719–729. https://doi.org/10.1139/t09-134.
Zhou, G.G.D., Cui, P., Chen, H.Y., Zhu, X.H., Tang, J.B., Sun, Q.C., 2013. Experimental study on cascading landslide dam failures by upstream flows. Landslides 10 (5), 633–643. https://doi.org/10.1007/s10346-012-0352-6.
Zhou, G.G.D., Cui, P., Tang, J.B., Chen, H.Y., Zou, Q., Sun, Q.C., 2015. Experimental study on the triggering mechanisms and kinematic properties of large debris flows in Wenjia gully. Eng. Geol. 194, 52–61. https://doi.org/10.1016/j.enggeo.2014.10.021.
Zhou, X.Q., Chen, Z., Li, S., Wang, L., 2015. Comparison of sediment transport model in dam break simulation. J. Basic Sci. Eng. 23 (6), 1097–1108.